A Statistical Model for Quantification and Prediction of Cardiac Remodelling: Application to Tetralogy of Fallot

T. Mansi, I. Voigt, B. Leonardi, X. Pennec, S. Durrleman, M. Sermesant, H. Delingette, AM. Taylor, Y. Boudjemline, G. Pongiglione, and N. Ayache

***Abstract*—Cardiac remodelling plays a crucial role in heart diseases. Analysing how the heart grows and remodels over time can provide precious insights into pathological mechanisms, eventually resulting in quantitative metrics for disease evaluation and therapy planning. This study aims to quantify the regional impacts of valve regurgitation and heart growth upon the end-diastolic right ventricle (RV) in patients with tetralogy of Fallot, a severe congenital heart defect. The ultimate goal is to determine, among clinical variables, predictors for the RV shape from which a statistical model that predicts RV remodelling is built. Our approach relies on a forward model based on currents and a diffeomorphic surface registration algorithm to estimate an unbiased template. Local effects of RV regurgitation upon the RV shape were assessed with Principal Component Analysis (PCA) and cross-sectional multivariate design. A generative 3D model of RV growth was then estimated using partial least squares (PLS) and canonical correlation analysis (CCA). Applied on a retrospective population of 49 patients, cross-effects between growth and pathology could be identified. Qualitatively, the statistical findings were found realistic by cardiologists. 10-fold cross-validation demonstrated a promising generalisation and stability of the growth model. Compared to PCA regression, PLS was more compact, more precise and provided better predictions.**

***Index Terms*—Statistical Shape Analysis, Currents Shape Representation, Partial Least Squares, Canonical Correlation Analysis, Cardiac Remodelling, Tetralogy of Fallot**

I. Introduction

A. Clinical Motivation: Cardiac Remodelling

Cardiac remodelling plays a crucial role in the course of a heart disease and in the outcome of a therapy. Analysing how the heart grows and remodels over time can provide precious insights into pathological mechanisms, eventually resulting in quantitative metrics for disease evaluation and therapy planning. The intricacy of the biological phenomena involved in growth and the extreme variability in the evolution of the heart anatomy make the prediction of cardiac remodelling dauntingly complex. So far, only global cardiac indicators, like blood pool volumes, have been used to quantify pathological growth in clinics [1], [2]. If such approaches greatly contributed in the understanding of the problem, they poorly unravel the complex 3D remodeling.

In this article we investigate the long-term cardiac remodelling in repaired Tetralogy of Fallot (rToF). ToF is a severe congenital heart disease of the right ventricle (RV) and pulmonary arteries that requires surgical repair. Yet, pulmonary valves may be damaged by the intervention, resulting in chronic regurgitation, severe RV dilation and abnormal cardiac electrophysiology due to injuries in the conduction system and to the RV dilation [3]. A depolarisation time, measured as the duration of the QRS complex in the ECG, higher than $180\,ms$ is a major determinant for adverse clinical events [4]. Pulmonary valve replacement (PVR) reduces the risk of life-threatening events but choosing the right timing of that therapy is still controversial [1], [4], [5]. Early PVR may increase the risk of multiple re-interventions subsequent to implant dysfunction or heart remodelling. Conversely, late intervention may be useless as the RV is irreversibly damaged. It is therefore fundamental to understand, quantify and predict RV growth for the management of rToF patients

Contrary to the left ventricle (LV), RV anatomy is complex and varies a lot among rToF patients. As a result, only few works analysed the local 3D alterations of the RV anatomy in rToF [6]–[8], in contrast to the numerous analyses of more global clinical features [1], [5], [9]. In [6], the authors identified significant differences in the RV anatomy between rToF and controls. This study relied on 1D shape indices only despite the availability of 3D segmentations, with the risk of overlooking complex 3D alterations. In [7], the authors compared the volumes of three distinct RV compartments between rToF patients and controls. They identified different degrees of dilation for each compartment, suggesting a non-homogeneous 3D remodelling of the RV. It is therefore essential to analyse the complete 3D RV shape to characterise the morphological changes due to the pathology. In [8], the authors proposed a 4D active appearance model of the beating heart to distinguish patients from controls. They obtained excellent classification but they did not relate the shape modes with clinical features

T. Mansi (tommaso.mansi@tmansi.net), X. Pennec, H. Delingette and N. Ayache are with INRIA Sophia Antipolis, Asclepios Research Team, France; M. Sermesant is with INRIA Sophia Antipolis, Asclepios Research Team, France and with King's College London, Division of Imaging Sciences and Biomedical Engineering, St Thomas' Hospital, London, U.K.; I. Voigt is with Siemens Corporate Research, Image Analytics and Informatics, Princeton, NJ, U.S.A. and with the University of Erlangen-Nuremberg, Pattern Recognition Lab, Germany; S. Durrleman is with the University of Utah, Scientific Computing and Imaging Institute, Salt Lake City, U.S.A.; A.M. Taylor is with the UCL Institute of Cardiovascular Sciences and with the Great Ormond Street Hospital for Children, London, U.K.; Y. Boudjemline is with the Service de Cardiologie Pédiatrique, Assistance Publique des Hôpitaux de Paris, Hôpital Necker-Enfants Malades, Paris, France; B. Leonardi and G. Pongiglione are with the Ospedale Pediatrico Bambino Gesù, Rome, Italy.

to identify and quantify pathological shape patterns.

B. Technical Background: Studying Pathologies Through Shape Analysis

1) Computational Shape Analysis: In the last decade, consistent mathematical frameworks [10], [11] have been developed to analyse organ shapes [12] and to study their evolution over time [13], with particular focus on neuroscience. A first approach consists in using landmark correspondences and model their spatial variability [14]–[17]. When correspondences are not available or cannot be determined consistently, organ shapes are analysed by studying how a representative template of the population deforms within this population. The idea is not to look at the shapes *per se* but at the deformations that match the template to the observations [18].

Two strategies are available to create the template. The backward strategy models the template as the average of all the deformed observations plus some residuals, which account for the variability in the space of shapes [19], [20]. Such a template is efficiently computed from the observations but the parameters, especially the residuals, are difficult to identify from the data. The forward strategy deals with this limitation by reverting the model [21], [22]. An observation is a deformation of the template plus some residuals that account for features that are not captured by the template nor the deformations (typically topology changes, shape outliers due to image artefacts, etc.). Estimating the template is more complex as it requires that the shapes, deformations and residuals are represented in a consistent way. Yet, model parameters can be faithfully estimated from images and clinical data. The user has better control on the shape information to analyse, facilitating the interpretation of the statistical findings.

2) Identification of Pathological Shape Features: The major application of the above-mentioned frameworks has been to identify pathological shape features in populations of patients compared to controls (see [23] and references therein for instance). Nevertheless, that approach does not quantify how much the shape is altered subject to the pathology. A way to perform this task is to correlate the shapes with clinical features that measure the degree of illness, provided that a consistent framework for shape representation is available. In [24], the authors use PCA on correspondences calculated by non-linear registration to relate the modes of variation of bone shapes to biomechanical properties simulated with finite element methods. They could identify variations of bone stress due to changes in bone anatomy, driving the elaboration of patient-specific implant. In [25], the authors performed PCA on shape descriptors of scoliotic spines. Resulting modes were consistent with the established clinical classification. In a preliminary study [26], we showed that the forward approach proposed in [22] enables one to identify shape features related to the severity of the regurgitation in rToF patients. This article significantly expands our approach by quantifying how the RV shape changes with the severity of regurgitation measured by different clinical metrics.

3) Modelling of Heart Growth: The complexity of the biological processes that give rise to cardiac growth hampers its modelling. So far, proposed models focus on specific mechanisms only, like cardiac fibre realignment or myocardium thickening under specific external stimuli [27]–[29]. A deeper understanding of these complex biological processes is required to develop more comprehensive models.

In parallel, statistical approaches have been proposed to study organ shape evolution over time. The assumption is that modifications in organ shape reveal underlying structural and functional dysfunctions. Most of these studies use longitudinal data, where the patient is scanned several times [13], [30]–[33]. Nonetheless, the very large time scale of the cardiac growth considered in rToF makes the acquisition of longitudinal data challenging. In such situations, cross-sectional statistical designs can be preferred [34]. The shapes are regressed with a clinical feature that represents patient growth, like age. A major challenge related to this technique is that the dimensionality of the shape representation hampers the prediction power of the model. A standard solution is to regress on the principal components, as we did in [26]. Yet, this approach may not be optimal as the determination of the PCA space is based on the shapes only, it does not explicitly consider the growth variable. PCA modes with low variations, usually considered as noise and thus discarded, can be relevant to pathological growth. Partial Least Squares Regression (PLS) deals with this limitation by automatically extracting the modes that are simultaneously relevant to the shapes and growth. Widely applied in computational chemistry [35], PLS has been used in the functional imaging community to predict activation patterns related to specific cognitive activities [36], [37]. In medical imaging, PLS appeared only recently. It has been used to predict the cardiac motion from respiratory signals to improve cardiac image acquisition [38]. In [39], PLS was applied on the PCA shape modes of brain structures to predict the shape of one structure according to the shape of another one.

C. Aim of the Study

In view of assisting the cardiologists in quantifying the morphological changes related to rToF and in establishing the best timing for PVR, we aim to estimate a generative model of the heart growth in rToF. The idea is to relate the heart shapes to clinical metrics to identify the pathological shape features and to model how they evolve over time. Such a growth model could provide quantitative metrics of local changes in the cardiac anatomy and function that could predict the cardiac remodelling in a patient.

As a first step towards this aim, we relate in this article the RV shape at end-diastole (ED) to regurgitation severity and model its 3D remodelling over time. The RV shapes are analysed using the forward approach proposed by [22] and briefly described in Sec. II-A. This framework is particularly suited for statistical analyses as *i)* it does not require point correspondences; *ii)* template and deformations are computed simultaneously and consistently; and *iii)* model parameters are well-defined, the shape information to analyse is controlled by the user. Two studies are carried out in 49 retrospective patients. No controls are included. First, the main modes of

variations computed by PCA are related to different clinical features that quantify RV regurgitation (Sec. II-B). We could thus detect local effects of regurgitation on the RV shape. Second, we estimate a generative model of RV growth using PLS and canonical correlation analysis (CCA) (Sec. II-C). We obtained a first clinically relevant model of RV growth in rToF (Sec. III). 10-fold cross-validation showed a promising generalisation and stability of our model. Finally, common patterns between the two studies highlighted possible cross-effects between regurgitation and growth. These results open new ways to analyse the cardiac anatomy, as discussed in Sec. IV.

II. Methods

A. Unbiased Template of the Right Ventricle

The RV at end-diastole of $N = 49$ patients is segmented from cine-MRI as described in Sec. III-A. The first step of the analysis is to estimate a template of the RV surfaces, or shapes, using the forward approach proposed in [22][1]. This template serves as reference atlas to determine the deformations towards each individual shape. The RV surface $\mathcal{T}^i$ of a patient i is modelled as the sum of the template $\overline{\mathcal{T}}$ deformed by a diffeomorphism ϕ^i and some residuals ϵ^i that stands for the features that are not represented by the template nor the deformations:

$$\mathcal{T}^i = \phi^i.\overline{\mathcal{T}} + \epsilon^i$$

Currents are used to represent the variables in the same framework. Intuitively, the current of a surface is the flux of any 3D vector field $\omega \in W$ across that surface. Mathematically, currents are continuous linear mappings from a vector space W to $\mathbb{R}$. When W is generated by a Gaussian kernel $K_W(\mathbf{x},\mathbf{y}) = \exp(-\|\mathbf{x}-\mathbf{y}\|^2/\lambda_W^2)$ (W is a Reproducible Kernel Hilbert Space, r.k.h.s. of infinite dimension and K_W defines an inner product of W), the dual space of currents W^* is the dense span of basis elements $\delta_{\mathbf{x}}^{\mathbf{a}}$, called Dirac delta currents, defined at the spatial position $\mathbf{x}$ and with direction $\mathbf{a}$. In that framework, we can approximate the current $\mathcal{T}^i$ of a triangulated surface by the sum of the Dirac delta currents defined at the triangle barycentres $\mathbf{x}_k^i$ and oriented along the triangle normals $\mathbf{a}_k^i$, $\mathcal{T}^i = \sum_k \delta_{\mathbf{x}_k^i}^{\mathbf{a}_k^i}$ (Fig. 1). The residuals ϵ^i are modelled as random Gaussian currents.

The deformation ϕ^i is estimated using the Large Deformation Diffeomorphic Metric Mapping (LDDMM) algorithm on surfaces presented in [40]. ϕ^i derives from a time-varying velocity field that is uniquely characterised by the initial velocity $\mathbf{v}_0^i$, which belongs to a Gaussian r.k.h.s. V with kernel K_V. $\mathbf{v}_0^i$ is parameterised by moment vectors $\beta_{\mathbf{x}_k}^i$ centred at the positions $\mathbf{x}_k$ of the delta currents of the template $\overline{\mathcal{T}}$ (Fig. 1):

$$\mathbf{v}_0^i(\mathbf{x}) = \sum_k K_V(\mathbf{x}_k,\mathbf{x})\beta_{\mathbf{x}_k}^i$$

The template $\overline{\mathcal{T}}$ and the deformations ϕ^i are estimated simultaneously with an alternate minimisation strategy based on step-varying gradient descent and initialised with the mean current of the population. The reader is referred to [22] for further details.

[1]The source code of the framework is freely available from http://www-sop.inria.fr/asclepios/projects/Health-e-Child/ShapeAnalysis/index.php

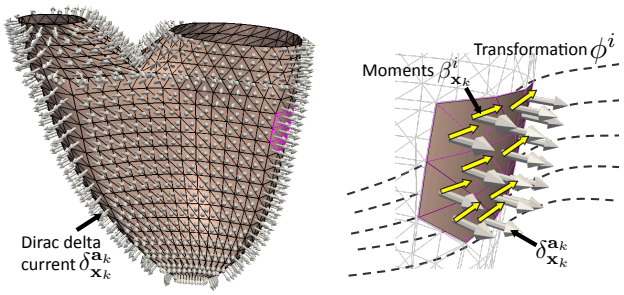

Fig. 1. The Dirac delta currents $\delta_{\mathbf{x}_k}^{\alpha_k}$ of a triangulated mesh are positioned at the barycentres $\mathbf{x}_k$ of every triangle and oriented along their normal. The moments $\beta_{\mathbf{x}_k}^i$ that parameterise the diffeomorphic deformation ϕ^i are defined at the $\mathbf{x}_k$'s. They are not necessarily normal to the surface.

The presented shape analysis algorithm has two parameters: the kernel width of the currents space, λ_W^2, and the kernel width of the velocity space, λ_V^2. They distribute the shape information between the deformations ϕ^i and the residuals ϵ^i. λ_W^2 controls the level of shape details to study. The larger λ_W^2, the more "blurry" the shape representation and the less details are considered. λ_V^2 controls the smoothness of the velocity fields, and thus of the transformations. Intuitively, λ_V^2 sets the size of the spatial region that is deformed consistently, i.e. the "rigidity" of the diffeomorphic transformation. Global shape differences are investigated using large λ_V^2, and *vice versa*.

For this study, we focused on the regional pathological features of the RV shape. We thus considered the shape information encoded by the deformations ϕ^i only. We do not analyse the residuals ϵ^i, which may be more challenging as shapes may have local inconsistencies due to the image artefacts often present in cine MRI. A major difficulty to address is the large dimensionality of ϕ^i, which is parameterised by thousands of moment vectors $\beta_{\mathbf{x}_k}^i$. A lot of patients would be necessary to get statistical significance. We deal with this difficulty by projecting the deformations ϕ^i onto subspaces well suited for the statistical analyses to perform.

B. Characterising Deformation Modes of the RV Shape

We first relate the shape to clinical indices in order to identify pathological shape patterns. To that end, a compact and intrinsic shape representation is computed by projecting the deformations onto an optimal PCA subspace. The resulting shape representation is tested with standard statistical designs.

1) Model Reduction on PCA Components: The initial velocities $\mathbf{v}_0^i$ of the deformations are projected onto a subspace computed using PCA. For computational efficiency, PCA is performed in the space of the observations, as the number of subjects N is usually smaller than the number of parameters of the velocities. Let $\mathbf{t}^m$ be the sorted principal components

of the $N \times N$ covariance matrix $\Sigma = (\sigma_{i,j})$,

$$\begin{aligned}\sigma_{ij} &= < \mathbf{v}_0^i - \overline{\mathbf{v_0}}, \mathbf{v}_0^j - \overline{\mathbf{v_0}} >_V \\ &= \sum_{\mathbf{x}_k, \mathbf{x}_l} (\beta^i_{\mathbf{x}_k} - \overline{\beta}_{\mathbf{x}_k})^T K_V(\mathbf{x}_k, \mathbf{x}_l)(\beta^j_{\mathbf{x}_l} - \overline{\beta}_{\mathbf{x}_l})\end{aligned}$$

In the previous equation, $\overline{\mathbf{v}_0}$ is the mean initial velocity, $\overline{\beta}_{\mathbf{x}_k}$ the average moment vector at the spatial position $\mathbf{x}_k$ and the superscripts i and j denote two different subjects. By construction, the component $\mathbf{t}^m$ belongs to the space of the observations. Thus, the m^{th} deformation mode, and more precisely the moment vector $\mathbf{p}^m$ that parameterises its initial velocity $\mathbf{v}_0^m$, is computed with the reconstruction formula $\mathbf{p}^m = \sum_i \mathbf{t}^m[i](\beta^i - \overline{\beta})$, where β^i contains all the moments related to ϕ^i and $\overline{\beta}$ is the average moment vector. The first p modes that explain at least $\pi\%$ of deformation variability are selected. By projecting the deformations ϕ^i's onto the resulting PCA subspace, we represent a subject by a low-dimensional shape vector $\mathbf{f}^i_{PCA} = \{f^{i,m}_{PCA}\}_{m=1..p}$ whose elements are the K_V-scalar products between $\mathbf{v}_0^i$ and the m^{th} mode $\mathbf{v}_0^m$.

2) Identification of Pathological Shape Features: The $f^{i,m}_{PCA}$'s quantify the amount of variability along the m^{th} mode that is present in the deformation ϕ^i. We thus investigate the RV shape by relating the shape vector $\mathbf{f}^i_{PCA}$ to clinical parameters that quantify the pathology. Ordinal clinical parameters are investigated using rank-based statistics. Kruskal-Wallis analysis of variance is applied to find effects between the investigated parameter and shape [41]. If an effect is found, post-hoc two-sample Wilcoxon test is used to determine which levels differ [41]. Continuous clinical parameters are investigated using linear regression and Akaike Information Criterion (AIC) model reduction [42] to detect relevant modes and the direction of correlation. All the tests were done with *R* [41]. The level of significance was set at $p < 0.1$. Multiple comparisons were corrected using Bonferroni adjustment.

C. A Generative Statistical Model of the RV Growth

In the second study, we investigate the RV growth through cross-sectional regression between observed RV shapes and body surface area (BSA), a continuous index of patient physiology computed from height and weight [43]. In paediatrics, BSA correlates well with age. We seek a model that returns a template corresponding to the average RV shape for a given BSA. The underlying idea is to deform the template $\overline{\mathcal{T}}$ with a transformation that depends on the BSA. Directly calculating such a model is hampered by the dimensionality of the transformation to predict from the 1D predictor (the BSA). We thus revert the point of view. First, we project the deformations ϕ^i onto a subspace that *i)* optimises the converse model $BSA = g(\beta)$ and *ii)* is relevant to both deformation and BSA. Under these requirements, PCA may not be optimal as it does not explicitly consider the growth variable. We instead use Partial Least Squares (PLS) regression. The relationship is then reversed through CCA to get the generative model of RV growth.

1) Model Reduction on PLS Components: PLS regression combines PCA and linear regression between two sets of variables X and Y to find bases, the PLS components, of maximum variance and covariance [44]. If X is the matrix of the N moment vectors β^i and Y is the vector of the N BSA values, N being the number of patients, then PLS returns the deformation modes that have maximal variance and maximal covariance with BSA.

Let $\mathrm{X}_c = \mathrm{X} - \overline{\mathrm{X}}$ and $\mathrm{Y}_c = \mathrm{Y} - \overline{\mathrm{Y}}$ be the centred variables. PLS consists in finding the latent vectors $\mathbf{r}$ and $\mathbf{s}$ that verify $\max_{|\mathbf{r}|=|\mathbf{s}|=1} cov(\mathrm{X}_c\mathbf{r}, \mathrm{Y}_c\mathbf{s})$, with the additional conditions:

$$\mathrm{X}_c = \mathrm{T}\mathrm{P}^T + \mathrm{E} \quad (1)$$

$$\mathrm{Y}_c = \mathrm{U}\mathrm{Q}^T + \mathrm{F} \quad (2)$$

$$\mathrm{U} = \mathrm{T}\mathrm{D} + \mathrm{G} \quad (3)$$

In the previous equations, T and U are the orthonormal matrices of components, which belong to the space of the observations; P and Q are the matrices of loadings, or modes, defined in the space of moments; D is a diagonal weight matrix; and E, F and G are matrices of residuals. Eq. 3 models the linear relationship between deformation and BSA.

The latent vectors, the components and the modes are computed iteratively with the PLS1 algorithm [44] (Algo. 1 in the Appendix). The components are automatically ordered by decreasing variance and covariance between deformation and BSA [44]. Therefore, the first q modes of X_c span an optimal subspace that simultaneously explain $\pi_X\%$ of the population shape variance and $\pi_Y\%$ of the population BSA variance. By projecting the deformations onto that subspace, we represent a subject by a low-dimensional PLS shape vector $\mathbf{f}^i_{PLS} = \{f^{m,i}_{PLS}\}_{m=1...q}$ whose elements are the scalar products between the moments β^i and the m^{th} PLS mode.

2) A Generative Model of the RV Growth: We then estimate the generative model of RV growth with canonical correlation analysis (CCA) between PLS shape vectors $\mathbf{f}^i_{PLS}$ and BSA. Intuitively, CCA estimates how much we should move along each PLS mode when BSA varies. This information can thus be used to calculate the deformation that must be applied to the template $\overline{\mathcal{T}}$ to get the average shape at a given BSA.

CCA generalises the notion of scalar correlation to sets of variables to find bases, the CCA components, of maximum correlation [45]. Let F be the $N \times q$ matrix of the PLS shape vectors $\mathbf{f}^i_{PLS}$ and Y the vector of BSA. CCA components are given by the SVD decomposition of the total covariance matrix

$$\Gamma(\mathrm{F}, \mathrm{Y}) = \mathrm{V}_{\mathrm{FF}}^{-1/2}\mathrm{V}_{\mathrm{FY}}\mathrm{V}_{\mathrm{YY}}^{-1/2} = \mathrm{R}\,\Omega\,\mathrm{S}^T$$

with $\mathrm{V}_{\mathrm{FF}} = \mathrm{F}^T\mathrm{F}/(N-1)$, $\mathrm{V}_{\mathrm{YY}} = \mathrm{Y}^T\mathrm{Y}/(N-1)$ and $\mathrm{V}_{\mathrm{FY}} = \mathrm{F}^T\mathrm{Y}/(N-1)$. Ω is the diagonal matrix of positive correlation coefficients between the components. R and S are the CCA components of the space of PLS shape vectors and BSA respectively.

As Y is a one-column matrix, Ω has only one non-null coefficient ω, which is the overall correlation between the PLS shape vectors and BSA. S equals ± 1, its sign determining the direction of correlation of BSA. The elements of the first column of R, denoted by ρ, relate to the amplitude and direction of correlation of each PLS mode when the BSA varies along the direction defined by S. More precisely, when the BSA is multiplied by x, we walk by $x\,S\,\omega\,\rho[k]$ along the

k^{th} PLS mode. Thus, if the RV template $\overline{\mathcal{T}}$ represents the RV shape at the population mean BSA, the RV template for a given BSA is obtained by deforming $\overline{\mathcal{T}}$ with the deformation $\Phi(\text{BSA})$ parameterised by the moments:

$$\beta(\text{BSA}) = \overline{\mathbf{b}} + \frac{BSA - \overline{\text{BSA}}}{\overline{\text{BSA}}} S\,\omega \sum_k \rho[k]\mathbf{p}^k \qquad (4)$$

where $\overline{\text{BSA}}$ is the average BSA of the population. The significance of the model is tested using Bartlett-Lawley test [46].

III. Experiments and Results

A. Data Collection

1) Subjects and Image Preparation: 49 patients with repaired ToF (33 males) were selected retrospectively from three hospitals based on their age (from 10 to 27 years) and their pulmonary regurgitation fraction (PRF $\geq 10\%$), none of which have undergone valve replacement (Table I). In that population, BSA [43] significantly correlated with age ($R^2 > 0.5$, $p < 5.10^{-4}$), justifying the use of that metrics to quantify patient growth. Steady-State Free Precession (SSFP) cine MRI of the heart were acquired with 1.5T MR scanners (Avanto, Siemens and Achieva, Philips) in the short-axis view, covering entirely both ventricles ($10-15$ slices; isotropic in-plane resolution ranging from $1.1 \times 1.1\,mm^2$ to $1.7 \times 1.7\,mm^2$; slice thickness: $5-10\,mm$; $25-40$ phases). PRF, defined as the percentage of backward pulmonary blood flow with respect to the outward flow, was estimated using 2D+t flow MRI acquired at the proximal pulmonary artery section. In 46 patients, end-diastole volume (EDVi), end-systole volume (ESVi) and pulmonary regurgitant volumes (PRVi $=$ PRF$\times$(EDVi$-$EDVi)), all indexed over BSA (values were divided by BSA to remove the effect of growth) were calculated from manual delineations of the RV endocardium. Finally, one rater assessed trans-pulmonary valve (TPVReg) and tricuspid (TriReg) regurgitation with one colour Doppler measurement (sweep speeds: $50-100\,mm/s$). 45 patients were classified with mild (7), moderate (15) and severe (23) TPVReg. Among them, 36 patients were classified with none (9), trace (4) and mild (23) TriReg.

TABLE I
Mean ± standard deviation of the main clinical features of 49 rToF patients (Values with * are calculated from 46 patients)

Age	17.2 ± 4.34 year
Body Surface Area (BSA)	$1.60 \pm 0.33\ m^2$
Indexed End-Diastole Volume (EDVi)	$155 \pm 49\,mL/m^{2*}$
Indexed End-Systole Volume (ESVi)	$86 \pm 34\,mL/m^{2*}$
Pulmonary Regurgitation Fraction (PRF)	$40 \pm 12\%$
Indexed Pulmonary Regurgitation Volume (PRVi)	$29 \pm 14\,mL/m^{2*}$

2) Surface Mesh Preparation: We studied the RV shape at end-diastole, when the anatomical features of the pathology are the most evident [6]. The RV endocardium was segmented on the cine MRI cardiac sequence by fitting an anatomically accurate geometrical model [47], [48]. Its position, orientation and scale in the end-diastole image was determined automatically using marginal space learning [47], which utilised a probabilistic boosting tree (PBT [49]) for classification in combination with Haar-like and steerable features. Then, boundaries were estimated locally using a PBT trained on steerable features in conjunction with a statistical shape model [14]. Manual refinement of the fitting was done if necessary. In order to restrict the variance across the data set to the differences in shape morphology for our analyses, the resulting RV meshes were rigidly aligned to a common coordinate frame. A standard least square method [50] was employed as mesh point correspondence among the segmentations was guaranteed with geometrical resampling in local anatomical coordinates (Fig. 2, left panel). Fig. 3 shows the RV components considered in the following analyses.

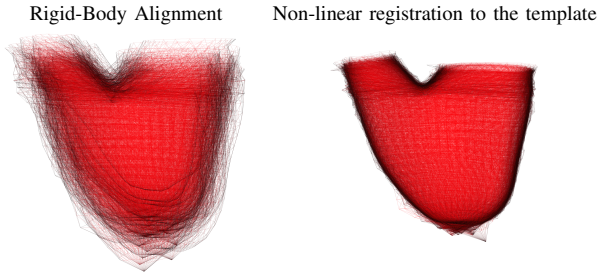

Fig. 2. 3D RV meshes of 49 rToF patients. *Left panel*: The meshes were rigidly aligned to a representative patient of the dataset. Observe the large variability in shape. *Right panel*: The same meshes registered back to the template using the diffeomorphic non-linear deformations.

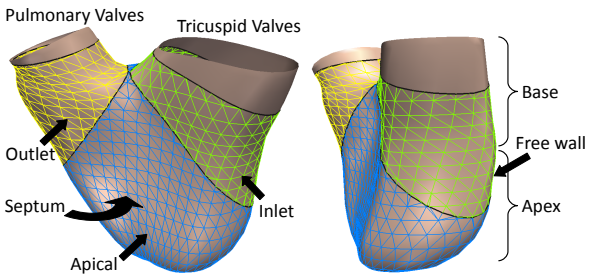

Fig. 3. RV anatomical components of a typical rToF patient.

B. Statistical Template of the Right Ventricle

1) Template Estimation: Estimating the RV template $\overline{\mathcal{T}}$ required setting the "rigidity" λ_V^2 of the diffeomorphic deformation and the resolution of the currents representation λ_W^2. As we were mainly interested in the regional alterations of the RV in rToF, λ_V^2 was set to $30\,mm$, about the diameter of the pulmonary annulus, and λ_W^2 to $10\,mm$, to have good mesh matching while discarding features due to image artefacts. Lower λ_W^2 values would have been inappropriate anyway as the image slice thickness was $\approx 10\,mm$.

The template estimation algorithm iterated four times, yielding a fairly well centred template in terms of velocities (standardised mean of velocities, $mean/sd = 0.4$). Most of the shape variability visible after linear registration were captured by the diffeomorphic template-to-subject transformations (Fig. 2). Remaining differences were mostly due to segmentation artefacts, thus not relevant for our analyses.

Interestingly, the age of the closest patient to the template, in terms of the current W-norm, was 16 and his BSA was $1.64\,m^2$. Both indices were fairly close to the population averages (Table I). In this population, the mean shape was consistent with the mean age and BSA.

2) Template Stability with Respect to the rToF Population: 10-fold cross-validation was performed to evaluate the stability of the template with respect to the rToF population. The 49 patients were randomly split into ten different groups of five (one with four) patients. Nine groups were used to estimate the RV template (training patients). The remaining group was used to test the model (test patients). That procedure resulted in ten different templates, henceforth denoted $\overline{\mathcal{T}}_k$. Unfortunately, two of them had to be discarded because the algorithm got trapped in local minima and did not converge properly (standardised mean of deformation velocities higher than 1.0). The other eight templates required from 1 to 8 iterations to converge (median $= 7$) and were well centred ($mean/sd = 0.36 \pm 0.24$).

Ideally, the $\overline{\mathcal{T}}_k$'s and the full-data template $\overline{\mathcal{T}}$ should be identical. We verified this assumption by calculating the standard deviation of the distances $d_W(\overline{\mathcal{T}}_k, \overline{\mathcal{T}})$, $\forall k$, in the space of currents W, which should be equal to the theoretical value, $\sigma/\sqrt{N}$ (σ is the standard deviation of the distances between the patients and the template $\overline{\mathcal{T}}$, $N = 49$ is the total number of patients). This simple rule provided a good indication of how much the template varied with respect to the population. Calculations yielded $\text{std}(d_W(\overline{\mathcal{T}}_k, \overline{\mathcal{T}})) = 34$, which was of the same order of magnitude than $\sigma/\sqrt{N} = 48$. This confirmed a good stability of the template with respect to the population, which could be verified visually (Fig. 4). Very small differences were visible between $\overline{\mathcal{T}}$ and $\overline{\mathcal{T}}_k$, $\forall k$ (average point-to-point distance: $1.2 \pm 0.4\,mm$).

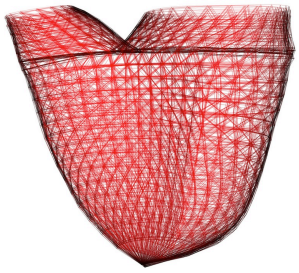

Fig. 4. Nine templates computed from nine different populations. The templates were very similar, no significant differences were visible. Average point-to-point distance: $1.2 \pm 0.4\,mm$.

C. Relating RV Shape to Regurgitation in rToF

Relationships between RV shape and pulmonary regurgitation were investigated by relating the PCA shape vectors $\mathbf{f}^i_{PCA}$ with TriReg, TPVReg and PRVi indices. 90% of the spectral energy was explained by 18 PCA modes, resulting in 18-element PCA shape vectors.

Kruskal-Wallis analysis showed a significant effect of tricuspid regurgitation (TriReg) on the deformation modes 11 ($p < 0.05$) and 15 ($p < 0.1$). According to pair-wise Wilcoxon test, these modes could separate trace from mild TriReg levels ($p < 0.05$ and $p < 0.1$ respectively). Visually (Fig. 5), both modes captured an elongation of the tricuspid annulus. Mode 11 encoded an enlargement of the apex whereas mode 15 displayed a bulging of the basal free-wall, both features resulted in a more rectangular RV shape.

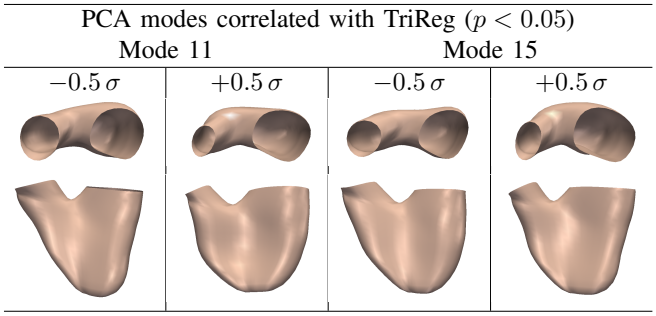

Fig. 5. PCA deformation modes related to tricuspid regurgitation (TriReg). The modes mainly captured an elongation of the tricuspid valve associated with a more rectangular shape of the ventricle. Both modes separated trace and mild TriReg ($p < 0.05$ and $p < 0.1$ respectively). Range of displayed deformation amplitude set at population variability.

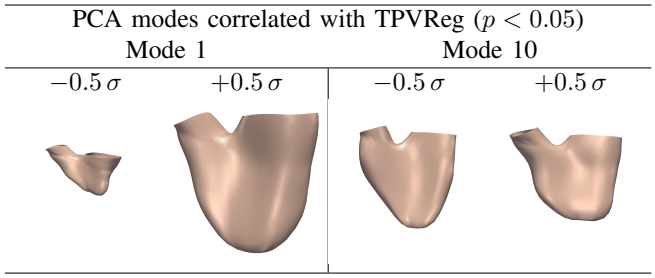

Fig. 6. PCA deformation modes related to transpulmonary regurgitation (TPVReg). Mode 1 showed an RV dilation whereas mode 10 exhibited a deformation of the RV base and bulging of the outlet. Analysis with pulmonary regurgitation volumes (PRVi) suggested that when PRVi increases, the RV dilates (mode 1 positively correlated) and the outlet bulges (mode 10 negatively correlated). Range of displayed deformation amplitude set at population variability.

The analysis of TPVReg revealed a significant effect of pulmonary regurgitation on the modes 1 ($p < 0.05$), 9 ($p < 0.1$), 10 ($p < 0.05$) and 12 ($p < 0.1$) but only the modes 1 and 10 could differentiate different levels (moderate/severe for mode 1, $p < 0.05$; mild/moderate for mode 10, $p < 0.1$). Visually (Fig. 6), mode 1 captured a dilation of the RV. Mode 10 exhibited a strong deformation of the valves and a localised dilation of the RV outlet.

These findings were confirmed by analysing the indexed pulmonary regurgitation volumes (PRVi) through linear regression ($\text{PRVi} = c + \sum_l a_l \mathbf{f}_{PCA}[l]$). The optimal linear model returned by AIC criterion consisted of nine PCA modes (Table II) and had a significant fit ($R^2 = 0.55$, $p < 5.10^{-4}$). Interestingly, the modes 1 and 10 were those with maximal significance to the linear model, suggesting a promising stability of our analysis as the same shape features were identified by two different parameters. The sign of the regression coefficient of mode 1 was positive. When PRVi increases, the 1^{st} mode goes towards $+\sigma$, i.e. the RV dilates (Fig. 6). In other words, the more severe the regurgitation, the more dilated the ventricle independently of growth (as values were indexed over BSA). Correlating the RV EDVi manually

measured with PRVi confirmed this finding (Fig. 7, Pearson's correlation coefficient $R = 0.67$, $p < 5.10^{-7}$) [5], [9]. Yet, here we got more information. In particular, the negative coefficient of mode 10 revealed that the outlet bulges (towards $-\sigma$) as regurgitation increases, suggesting a localised impact of regurgitation on the RV shape. Finally, we noticed that mode 11 was also relevant to PRVi, which may suggest possible cross-effects between pulmonary and tricuspid regurgitation.

TABLE II
REGRESSION COEFFICIENTS a_l BETWEEN PCA SHAPE VECTORS AND PRVI AFTER AIC REDUCTION ($R^2 = 0.55$, $p < 5.10^{-4}$). THE SIGN INDICATES THE DIRECTION OF THE MODES FOR INCREASING PRVI.

	c	a_1	a_2	a_4	a_5
Coef. $\times 10^{-2}$	3130	0.23	-0.58	1.05	0.74
p-value	2.10^{-20}	3.10^{-4}	0.04	0.006	0.114
	a_7	a_9	a_{10}	a_{11}	a_{18}
Coef. $\times 10^{-2}$	1.61	-1.28	-3.27	-1.86	3.33
p-value	0.004	0.11	5.10^{-4}	0.05	0.09

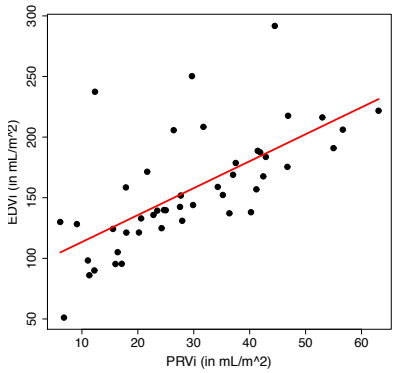

Fig. 7. Evolution of RV EDVi with respect to PRVi ($R = 0.67$, $p < 5.10^{-7}$). The larger the regurgitant volume, the more dilated the ventricle, which confirmed the relevance and the positive correlation of the PCA Mode 1 with pulmonary regurgitation (Fig. 6).

D. Statistical Model of RV Growth in Repaired ToF

1) PLS Model of RV Growth: The nine first PLS modes explained 98% of the BSA variability and 56% of the shape variability observed in our population. By construction, the PLS modes evolved towards $+\sigma$ when BSA increased. Their relevance to BSA was confirmed through linear regression between the PLS shape vectors $\mathbf{f}^i_{PLS}$ and BSA (BSA $= g_{PLS}(\mathbf{f}_{PLS}) = c + \sum_l a_l \mathbf{f}_{PLS}[l]$). All the modes were significant to the linear model ($p < 0.05$), thus to BSA, and kept by AIC criterion (Table III). The fit was very strong ($R^2 = 0.89$, $p < 10^{-15}$). It has to be noted that in that experiment we were mainly interested in the shape information that was relevant to BSA, and not in the total shape variability. This contrasts with the previous analyses that aimed to compare the RV shape to different clinical metrics.

As the template $\overline{\mathcal{T}}$ was consistent with the average BSA (Sec. III-B1), we computed the generative model of RV growth by deforming $\overline{\mathcal{T}}$ with the growth deformation $\Phi(\text{BSA})$ parameterised by (Eq. 4). CCA confirmed the strong correlation between the PLS modes and BSA (overall correlation $\omega = 0.95$, $p < 10^{-8}$). The individual canonical correlations $\rho[k]$ decreased exponentially (Fig. 8, left panel). The "time" constant of the fitted exponential was 1.96. After six modes the correlation with BSA was already 0.1.

TABLE III
REGRESSION COEFFICIENTS a_l BETWEEN PLS SHAPE VECTORS AND BSA ($R^2 = 0.89$, $p < 5.10^{-16}$). ALL THE PLS MODES WERE RELEVANT TO BSA AND POSITIVELY CORRELATED.

	c	a_1	a_2	a_3	a_4
Coef. $\times 10^{-4}$	1595	4.3	9.4	8.6	10.8
p-value	$< 2.10^{-16}$	$< 2.10^{-16}$	$< 2.10^{-16}$	10^{-14}	3.10^{-11}
	a_5	a_6	a_7	a_8	a_9
Coef. $\times 10^{-4}$	9.0	12.0	9.4	6.0	2.8
p-value	1.10^{-9}	6.10^{-8}	2.10^{-5}	7.10^{-4}	0.02

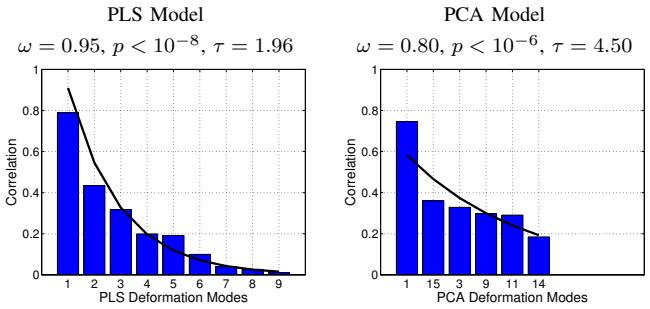

Fig. 8. CCA correlation coefficients between BSA and PLS/PCA modes. *Black line*: fitted exponential. Contrary to PCA, PLS provided better correlation with BSA, the individual modes were automatically extracted by decreasing order of correlation. The decrease of the individual canonical correlations was much faster (lower time constant τ), denoting a lower spread of the shape information relevant to BSA over the modes.

The RV growth model was visually plausible (Fig. 9). As BSA increased, RV volume increased while the free-wall, the tricuspid valves and the outlet dilated. In proportion, the apex dilated more and faster than the inlet and outlet (Fig. 10). That result follows the observations reported in [7], who identified significantly different end-diastolic volumes of the apical components between rToF patients and controls, whereas inlet and outlet end-diastolic volumes were not significantly different between the two groups. The septum of our model stayed relatively flat as BSA increased. Expected by the cardiologists involved in the project, that behaviour could be explained by the pressure overload often reported in rToF patients [6], [51].

2) Generalisation of the RV Growth Model: Generalising the statistical model of RV growth is of primary importance for patient management and therapy planning. Ideally one would like to predict the RV shape of a patient from a BSA. However, this challenging task would require longitudinal data, which are challenging to obtain for rToF due to the large time scale of the pathology. We thus tested the RV growth model by predicting patients' BSA from their RV shape. Although such an application has little clinical relevance, it enables one to evaluate the ability of the model to represent new patients.

We predicted the BSA of 39 patients from the templates $\overline{\mathcal{T}}_k$ given by the above-mentioned 10-fold cross-validation technique (ten patients were discarded as the respective tem-

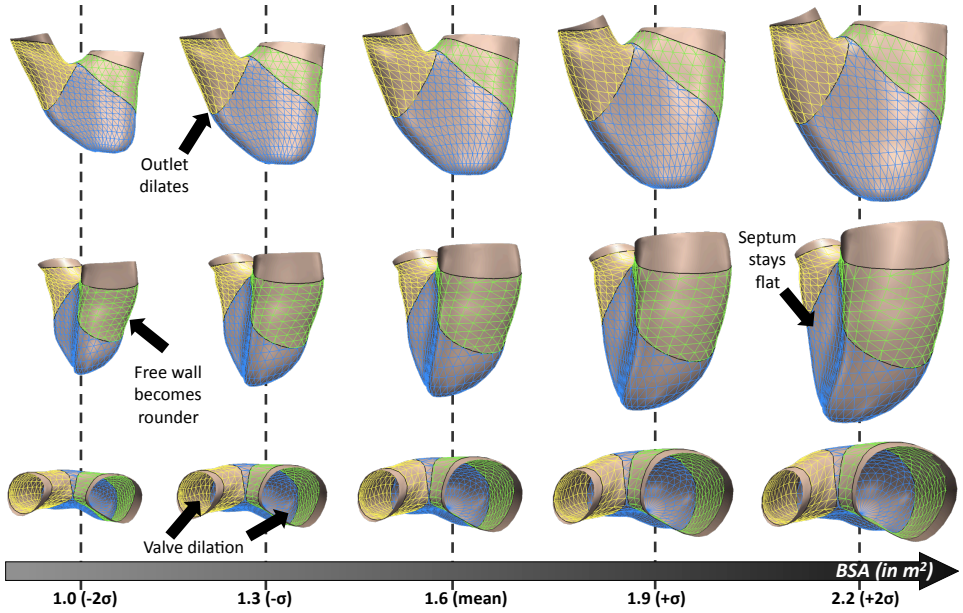

Fig. 9. Average RV growth computed from a population of 49 rToF patients. While BSA increases, RV globally enlarges, in particular the apical component. Simultaneously, the valves significantly dilate, the free wall becomes rounder but the septum stay relatively flat. At high BSA, RV outlet becomes rounder.

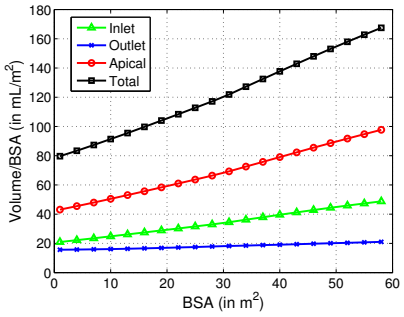

Fig. 10. Evolution of the indexed volumes of each RV component. The apical component dilated faster than the other components in our model. The outlet was the least affected component while the inlet dilated mainly because of the bulging of the free-wall. These findings were consistent with [7].

plates did not converge). The PLS shape vectors of the training patients related to $\overline{\mathcal{T}}_k$ were used to estimate the linear model $\text{BSA} = g_{PLS_k}(\mathbf{f}_{PLS})$, which was then applied to predict the BSA of the test patients. 95% prediction interval was also calculated to assess the precision of the predictions.

In average, BSA was successfully predicted. The mean error ($0.26 \pm 0.22\, m^2$) and median error ($0.20\, m^2$) were below population SD ($0.33\, m^2$). 95% prediction interval was also satisfying ($0.23 \pm 0.03\, m^2$), considering the large variability of RV shapes in rToF patients. Fig. 11 reports the individual predictions. If for the majority of patients the prediction error is below population SD, the BSA of 12 patients could not be predicted. By comparing their RV end-diastolic volume with their BSA, we found that six of these patients were clear outliers (Fig. 11, right panel). Their RV was larger or smaller than in average. This difference may suggest a fast deterioration of the RV or, conversely, a protection to the disease. The model could therefore be used to distinguish patients that deviate from the "average" rToF growth. BSA prediction also failed for patients with low BSA, although they were relatively close to the average trend. A possible reason for that is the few number of subjects in that range of BSA.

3) Comparison with PCA Regression: In [26], we built the growth model by applying CCA on the PCA modes that were found relevant to the linear regression $\text{BSA} = c + \sum_l a_l \mathbf{f}_{PCA}[l]$. In our population, six PCA deformation modes were found relevant to BSA, with good fit ($R^2 = 0.64, p < 5.10^{-8}$) (Table IV). Less modes were required to generate the growth model than with PLS, but only 47% of shape variability was captured (56% by the PLS modes).

TABLE IV
REGRESSION COEFFICIENTS a_l BETWEEN PCA SHAPE VECTORS AND BSA AFTER AIC MODEL REDUCTION ($R^2 = 0.64, p < 5.10^{-8}$). SIX MODES WERE KEPT. THE SIGN INDICATES THE DIRECTION OF CORRELATION FOR INCREASING BSA.

	c	a_1	a_3	a_9	a_{11}	a_{14}	a_{15}
Coef. $\times 10^{-4}$	1595	0.7	−1.5	3.3	3.8	3.3	7.6
p-value	$< 2.10^{-16}$	7.10^{-8}	0.007	0.01	0.02	0.12	0.003

CCA returned a less correlated model with PCA ($\omega_{PCA} = 0.80$). Moreover, as theoretically expected, the individual correlations $\rho[k]$ between the PCA modes with BSA did not depend on their variance (Fig. 8, right panel). Some modes with low variance (e.g. mode 15) were more correlated with BSA than first modes, (e.g. mode 3). Artificial cut-off on the cumulated variance can discard PCA modes with low variance but highly related to the clinical parameter of interest. In addition to that, the $\rho[k]$, ordered by decreasing correlation, did not decrease as fast as the PLS coefficients. As shown in Fig. 8, four PCA modes were similarly correlated with BSA. The shape information relevant to growth were equally spread over these modes. In contrast, PLS automatically extracted

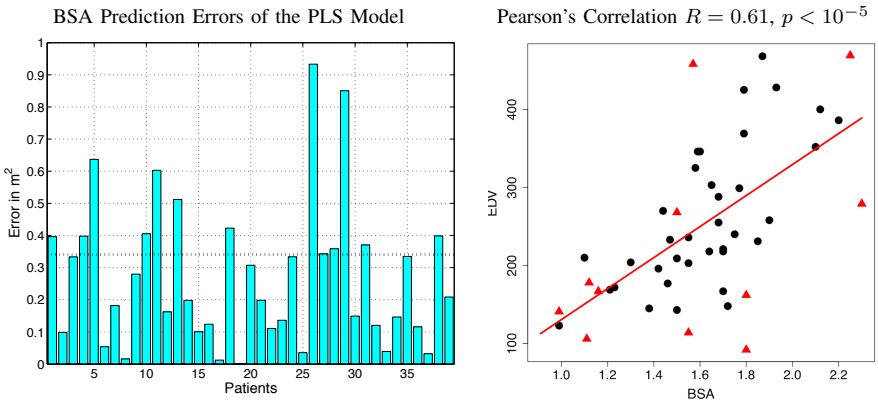

Fig. 11. *Left panel:* Errors of the predicted BSA calculated from the RV shapes of the tested patients using the PLS model. In average, the errors compared fairly well with population BSA ($error = 0.26\,m^2$, std(BSA) $= 0.33\,m^2$), with a 95% prediction interval ($0.23\,m^2$) below population SD. *Right panel:* non-indexed RV EDV with respect to BSA. Patients for which BSA prediction failed are in red triangles. Except one patient for which the model failed without clear explanation, most of them are outliers (RV size significantly larger or smaller than the average) or small patients. For the later cases, the prediction failed probably because of the small number of patients with similar BSA *(See text for details)*

modes whose correlation with BSA decreased exponentially, automatically ordered by covariance and correlation.

Finally, we evaluated the prediction power of the PCA model by calculating the BSA of the test patients from their PCA shape vector. Like the PLS model, predicted BSA were satisfying in average ($error = 0.23 \pm 0.19\,m^2$, median $= 0.18\,m^2$). However, the 95%-prediction interval was twice as large as the PLS one ($0.46 \pm 0.04\,m^2$), higher than population SD. Predicted values were therefore much less precise. The PLS model could therefore better represent new patients.

E. Cross-Effects Between Regurgitation and Growth

We finally investigated the cross-effects between growth and pulmonary regurgitation on the RV shape by correlating the PLS shape vectors with TPVReg and PRV. Non-indexed measures were used as growth is now part of the analysis. A significant effect was found between TPVReg and the 1^{th} and 2^{nd} PLS modes (Fig. 12). These modes were also found relevant to PRV, with positive and significant ($p < 0.05$) regression coefficients. The 1^{th} PLS mode was strikingly similar to the 1^{th} PCA mode. It encoded a global dilation of the RV. The 2^{nd} PLS mode showed some features common to the 10^{th} PCA mode (Fig. 6), especially the progressive bulging of the RV outlet. This analysis suggested a link between growth, dilation and severity of pulmonary regurgitation.

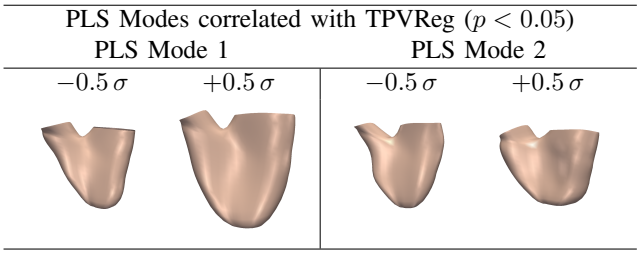

Fig. 12. PLS modes related to pulmonary regurgitation (TPVReg). Correlation with PRV showed that these modes evolve towards $+\sigma$, in the direction of increasing BSA, when PRV increases. The RV dilates and the outlet bulges. They were similar to PCA modes 1 and 10, also found relevant to PRV. These trends may highlight cross-effects between growth and regurgitation on the RV shape. Range of displayed deformation amplitude set at population variability.

IV. Discussion and Conclusion

We have presented in this article a new way to investigate the 3D changes of the heart shape related to rToF. We related clinical parameters to the RV shape at end-diastole, when the effects of the pathology on the anatomy are the most evident, to identify pathological shape patterns and quantify the RV remodelling in 49 rToF patients. Contrary to previous clinical studies that rely on global parameters such as blood pool volume, we quantify in this work regional, localised anatomical changes and their evolution over time. An ideal template was estimated from the population using currents shape representation and LDDMM registration algorithm. Multivariate statistical analyses on the deformations highlighted global and regional shape features related to the severity of regurgitation and provided a generative model of the observed RV growth. The findings were clinically relevant as they exhibited realistic changes in RV anatomy previously reported in the literature [6], [7]. To the best of our knowledge, the present study constitutes a first attempt at combining currents-based shape analysis methods with statistical designs like PLS to quantify the pathological 3D RV shape in rToF and to estimate a generative model of RV growth in that population. These analyses may yield quantitative image-based indices about RV anatomy and remodelling in ToF.

We first estimated an RV template from the observed shapes. That template was well centred and stable with respect to the population of reference. 10-fold cross validation showed that the template did not change significantly when the dataset varies. Non-reported 3-fold cross validation resulted in similar conclusions (average point-to-point distance: $1.4 \pm 0.5\,mm$). This encouraging result suggests a promising generalisation of the statistical findings. Our template could be used for other analyses, on other rToF patients, without re-estimating it.

The effects of regurgitation severity measured from colour Doppler ultrasound were analysed on a component-by-

component basis to preserve the statistical power of the tests due to the ordinal nature of the information obtained from ultrasound. The groups were not sufficiently populated to apply more comprehensive statistics. Despite this limitation, selected PCA deformation modes were clinically relevant and consistent with the modes exhibited by multivariate regression between RV shape and pulmonary regurgitation volumes, which considers all the modes at the same time and provides the direction of correlation. We could thus identify that the RV dilates, the outlet bulges and the apex deforms as regurgitation becomes worse and the child grows. These findings were consistent with reported observations in the literature and our previous studies [26], [52]. Indeed, despite the different ordering of the PCA modes, which depends on the population, the modes that were statistically related to the clinical features were fairly consistent between the studies (we refer the reader to the figures reported in [26], [52]). One could quantify the similarity between PCA subspace (using cosine betwen modes or bootstrapping approaches [53]) but the interpretation of the results is not straightforward.

The effects of growth on the RV shape were investigated using partial least squares (PLS) on the deformation moments. Contrary to PCA, PLS automatically finds the minimal yet optimal number of deformation modes that were simultaneously relevant to shape and BSA. PLS thus prevents the risk of discarding shape information relevant to growth but with low variance. Our model was realistic, with promising generalisation. It showed a progressive dilation of the RV, in particular at the free-wall and at the apex. The outlet dilates as the valves deform. Compared to PCA regression, the PLS model provided a more precise prediction, although all the patients could not be predicted by the model due to the large variability in RV anatomy. Those cases showed that the model could also be used to detect patients that deviate from the average rToF growth. Hence, patients that get worse with respect to the average rToF population could be detected and a PVR planned.

49 patients were used in this study. This number of subjects is sufficient for rank-based statistical tests, which can be performed on very small databases, as they do not assume any distribution. Moreover, according to the central limit theorem [54], 49 subjects should also be enough to fulfil the theoretical assumptions of PCA and linear regressions. This was confirmed by the very good statistical powers of our tests [55]. That said, 49 patients might not be enough in practice to represent the large anatomical variability in rToF. Although reported trends were consistent with previous works on smaller populations [26], [52], studies on larger multi-centric databases would be necessary to confirm these findings.

Our work opens several technical and clinical questions. From a technical point of view, the PLS model could be improved by considering the kernel properties of the space of velocity. We applied the PLS method on the moments although theoretically the L_2 scalar product between moments is ill-defined. Furthermore, the non orthogonality of the PLS loadings may yield multi-collinear shape vectors, which can hamper the prediction power of the model. A possible solution would be to perform PLS directly in the kernel space of velocities. The linear model may also be too restrictive. It is indeed acknowledged that the growth in teenagers follows a "sigmoidal" trend. A straightforward extension of our work is to fit polynomial or sigmoidal models to the data but a more elegant way to cope with this would be to perform kernel regression and kernel canonical correlation analysis in the space of velocities.

Another technical research direction is to apply the statistical model of RV growth to predict the RV shape of a specific patient, from group-wise analyses to patient-specific predictions. This can be achieved by "transporting" the deformation associated to the growth model to the patient RV anatomy [56]. However, this task is not trivial as it requires parallel transport algorithms tailored to the Riemannian manifold of diffeomorphisms [31], [57].

From a clinical point of view, relating RV shape with clinical features opens new ways to study key clinical questions related to rToF and other cardiac pathologies. First, it would be interesting to extend the current 3D framework to time series, to correlate the changes in shape and function with pathology and growth. A first approach would be to consider the shapes at ED and ES simultaneously, yielding a 2-column shape matrix instead of the shape vector used in this paper. Multivariate analyses would then be applied to highlight the pathological changes in cardiac morpho-dynamics. PLS can be applied directly as this method is also suitable for two sets of variables. Unfortunately, although the proposed framework enables it, we could not perform such a study because of the lack of the segmentations at ES. More sophisticated spatio-temporal approaches [30], [33], [56] could also be employed.

The LV-RV interactions such as septal deformation could also be investigated by creating models of the bi-ventricular myocardium. Our framework can be easily adapted to multi-label templates by co-registering the LV and the RV consistently such that the anatomical correspondence is preserved [22]. This could not be done in the population of that paper, as the LV segmentations were not available, but preliminary results in a different and much smaller population were promising.

In that article, we considered all the rToF patients who were available to maximise the power of the statistical analyses. Nonetheless, the type of initial repair may lead to different RV remodelling [9], [58]. It would be interesting to investigate how that repair influences the RV growth and pathology evolution by differentiating different groups of patients. Yet, this question is extremely difficult to tackle as surgical techniques vary amoung clinical centres and, above all, improve over time.

Recently, direct computational models of heart electromechanics and fluid dynamics have been investigated to simulate, *in-silico*, the postoperative effects of pulmonary valve replacement [59], [60]. These approaches showed promising results and could assist, in the future, the surgeon to plan the optimal intervention for a specific patient. However, they do not model the cardiac remodelling that follows the therapy, which can be as crucial as the therapy itself. A statistical approach like ours could go with these models to predict the long-term surgical outcomes. For a given PVR strategy, one would collect follow-up data and build the statistical model, which could then be

applied to the simulated postoperative heart to predict the long-term remodelling.

Other interesting clinical questions related to rToF could be investigated using our approach. For instance, there is nowadays a clinical consensus that a longer QRS duration correlates with RV dilation [3], [4]. Correlating this parameter with the RV shape could reveal how the abnormal conduction system impacts the RV anatomy and function. Similarly, studying body-mass index (BMI) jointly with BSA could provide a more comprehensive representation of the patient growth. One could apply the PLS method between two sets of multivariate variables (BMI, BSA and QRS on the one hand, the shape vectors on the other hand) and get a growth model that explains both features. Unfortunately, QRS durations and BMI were not available for all the patients as the population was retrospective, keeping these questions for future work.

The effect of genetic factors that regulate myocardium stiffness on the long-term RV remodelling could also be analysed. Patients with stiffer myocardium are known to be more protected against RV dilation. These patients may be the outliers of the model with "abnormally" smaller RV than the average. The decision for valve implant may be delayed and based on different features for these patients. Finally, group-wise analyses between patients and controls would further help in identifying pathological shape patterns. Unfortunately we could not do that, no healthy subjects were available.

In conclusion, we have presented in this article a method to quantitatively relate shapes to clinical features and model their evolution over time. The results on the RV shape in rToF patient encourages us to extrapolate the approach to the numerous clinical questions we discussed and to other cardiac pathologies involving cardiac remodelling.

APPENDIX

Algo. 1 summarises the main steps of the PLS1 algorithm, used to estimate the PLS shape components [44].

Algorithm 1 Partial Least Squares Regression (PLS1)

Require: Variables X and Y, Nb of components $p \leq N-1$.

$\mathrm{X}_c^0 = \mathrm{X} - \overline{\mathrm{X}}$, $\mathrm{Y}_c^0 = \mathrm{Y} - \overline{\mathrm{Y}}$
for $n = 1$ to p **do**
  $\mathbf{r}^n \leftarrow$ first eigenvector of ${\mathrm{X}_c^n}^T \mathrm{Y}_c^n {\mathrm{Y}_c^n}^T \mathrm{X}_c^n$
  $\mathbf{t}^n \leftarrow \mathrm{X}_c^n \mathbf{r}^n / \|\mathbf{r}^n\|$ {n^{th} *PLS component of* X}
  $\mathbf{s}^n \leftarrow {\mathrm{Y}_c^n}^T \mathbf{t}^n / ({\mathbf{t}^n}^T \mathbf{t}^n)$
  $\mathbf{u}^n \leftarrow \mathrm{Y}_c^n \mathbf{s}^n / \|\mathbf{s}^n\|$ {n^{th} *PLS component of* Y}
  $\mathbf{p}^n \leftarrow {\mathrm{X}_c^n}^T \mathbf{t}^n / ({\mathbf{t}^n}^T \mathbf{t}^n)$ {n^{th} *loading of* X}
  $\mathbf{q}^n \leftarrow {\mathrm{Y}_c^n}^T \mathbf{u}^n / ({\mathbf{u}^n}^T \mathbf{u}^n)$ {n^{th} *loading of* Y}
  $\mathrm{X}_c^{n+1} \leftarrow \mathrm{X}_c^n - \mathbf{t}^n {\mathbf{p}^n}^T$ {*deflation of* $\mathrm{X_c}$}
  $\mathrm{Y}_c^{n+1} \leftarrow \mathrm{Y}_c^n - \mathbf{t}^n [{\mathbf{t}^n}^T \mathrm{Y}^n / ({\mathbf{t}^n}^T \mathbf{t}^n)]$ {*deflation of* $\mathrm{Y_c}$}
end for
return $\mathrm{T} = (\mathbf{t}^n)_{n=1\ldots p}$, $\mathrm{P} = (\mathbf{p}^n)_{n=1\ldots p}$, $\mathrm{U} = (\mathbf{u}^n)_{n=1\ldots p}$, $\mathrm{Q} = (\mathbf{q}^n)_{n=1\ldots p}$

ACKNOWLEDGMENT

This work has been partly funded by the European Commission, IST-2004-027749 Health-e-Child Integrated Project. The authors warmly thank Boris Bernhardt, Neuroimaging Laboratory of Epilepsy, Montreal Neurological Institute, for his helpful comments about the statistical designs, and the reviewers for their constructive comments about this manuscript.

REFERENCES

[1] J. Therrien, Y. Provost, N. Merchant, W. Williams, J. Colman, and G. Webb, "Optimal timing for pulmonary valve replacement in adults after tetralogy of Fallot repair," *The American journal of cardiology*, vol. 95, no. 6, pp. 779–782, 2005.

[2] T. Oosterhof, "Cardiovascular magnetic resonance in patients with corrected Tetralogy of Fallot," Ph.D. dissertation, Unversity of Amsterdam, 2006.

[3] M. A. Gatzoulis, J. A. Till, J. Somerville, and A. N. Redington, "Mechanoelectrical interaction in tetralogy of Fallot : QRS prolongation relates to right ventricular size and predicts malignant ventricular arrhythmias and sudden death," *Circulation*, vol. 92, no. 2, pp. 231–237, 1995.

[4] R. Scherptong, M. Hazekamp, B. Mulder, O. Wijers, C. Swenne, E. van der Wall, M. Schalij, and H. Vliegen, "Follow-Up After Pulmonary Valve Replacement in Adults With Tetralogy of Fallot:: Association Between QRS Duration and Outcome," *Journal of the American College of Cardiology*, vol. 56, no. 18, pp. 1486–1492, 2010.

[5] T. Geva, "Indications and timing of pulmonary valve replacement after tetralogy of Fallot repair," in *Seminars in Thoracic and Cardiovascular Surgery: Pediatric Cardiac Surgery Annual*, vol. 9. Elsevier, 2006, pp. 11–22.

[6] F. Sheehan, S. Ge, G. Vick III, K. Urnes, W. Kerwin, E. Bolson, T. Chung, J. Kovalchin, D. Sahn, M. Jerosch-Herold *et al.*, "Three-Dimensional Shape Analysis of Right Ventricular Remodeling in Repaired Tetralogy of Fallot," *The American Journal of Cardiology*, 2007.

[7] N. Bodhey, P. Beerbaum, S. Sarikouch, S. Kropf, P. Lange, F. Berger, R. Anderson, and T. Kuehne, "Functional Analysis of the Components of the Right Ventricle in the Setting of Tetralogy of Fallot," *Circulation: Cardiovascular Imaging*, vol. 1, no. 2, p. 141, 2008.

[8] H. Zhang, A. Wahle, R. Johnson, T. Scholz, and M. Sonka, "4D Cardiac MR Image Analysis: Left and Right Ventricular Morphology and Function." *IEEE Transactions on Medical Imaging*, vol. 29, no. 2, pp. 350–364, February 2010.

[9] M. Samyn, A. Powell, R. Garg, L. Sena, and T. Geva, "Range of ventricular dimensions and function by steady-state free precession cine MRI in repaired tetralogy of Fallot: right ventricular outflow tract patch vs. conduit repair," *Journal of Magnetic Resonance Imaging*, vol. 26, no. 4, pp. 934–940, 2007.

[10] U. Grenander and M. Miller, "Computational anatomy: An emerging discipline," *Quarterly of applied mathematics*, vol. 56, no. 4, pp. 617–694, 1998.

[11] X. Pennec, "Statistical computing on manifolds: from Riemannian geometry to computational anatomy," in *Emerging Trends in Visual Computing*, ser. Lecture Notes in Computer Science. Springer, 2008, vol. 5416, pp. 347–386.

[12] J. Ashburner, C. Hutton, R. Frackowiak, I. Johnsrude, C. Price, and K. Friston, "Identifying global anatomical differences: deformation-based morphometry," *Human Brain Mapping*, vol. 6, no. 5-6, pp. 348–357, 1998.

[13] P. Thompson, J. Giedd, R. Woods, D. MacDonald, A. Evans, and A. Toga, "Growth patterns in the developing brain detected by using continuum mechanical tensor maps," *Nature*, vol. 404, no. 6774, pp. 190–193, 2000.

[14] T. Cootes, C. Taylor, D. Cooper, J. Graham *et al.*, "Active shape models-their training and application," *Computer vision and image understanding*, vol. 61, no. 1, pp. 38–59, 1995.

[15] A. Frangi, D. Rueckert, J. Schnabel, and W. Niessen, "Automatic construction of multiple-object three-dimensional statistical shape models: Application to cardiac modeling," *IEEE Transactions on Medical Imaging*, vol. 21, no. 9, pp. 1151–1166, 2002.

[16] M. Styner, J. Lieberman, D. Pantazis, and G. Gerig, "Boundary and medial shape analysis of the hippocampus in schizophrenia," *Medical Image Analysis*, vol. 8, no. 3, pp. 197–203, 2004.

[17] H. C. van Assen, M. G. Danilouchkine, A. F. Frangi, S. Ordas, J. J. Westenberg, J. H. Reiber, and B. P. Lelieveldt, "SPASM: A 3D-ASM for segmentation of sparse and arbitrarily oriented cardiac MRI data," *Medical Image Analysis*, vol. 10, no. 2, pp. 286–303, April 2006.

[18] D. Thompson, *On Form and Growth*. Cambridge University Press, 1917.

[19] A. Guimond, J. Meunier, and J.-P. Thirion, "Average brain models: A convergence study," *Computer Vision and Image Understanding*, vol. 77, no. 2, pp. 192–210, 2000.

[20] S. Joshi, B. Davis, M. Jomier, and G. Gerig, "Unbiased diffeomorphic atlas construction for computational anatomy," *NeuroImage*, vol. 23, pp. 151–160, 2004.

[21] S. Allassonniere, Y. Amit, and A. Trouve, "Towards a coherent statistical framework for dense deformable template estimation," *Journal of the Royal Statistical Society: Series B (Statistical Methodology)*, vol. 69, no. 1, pp. 3–29, 2007.

[22] S. Durrleman, X. Pennec, A. Trouvé, and N. Ayache, "Statistical models on sets of curves and surfaces based on currents," *Medical Image Analysis*, vol. 13, no. 5, pp. 793–808, Oct. 2009.

[23] J. Cates, P. Fletcher, and R. Whitaker, "A hypothesis testing framework for high-dimensional shape models," in *MICCAI Workshop on Mathematical Foundations of Computational Anatomy*, 2008, p. 170.

[24] L. Querol, P. Büchler, D. Rueckert, L. Nolte, and M. Ballester, "Statistical finite element model for bone shape and biomechanical properties," in *Medical Image Computing and Computer Assisted Intervention (MICCAI)*, ser. Lecture Notes in Computer Science. Springer, 2006, pp. 405–411.

[25] J. Boisvert, F. Cheriet, X. Pennec, H. Labelle, and N. Ayache, "Geometric variability of the scoliotic spine using statistics on articulated shape models," *IEEE Transactions on Medical Imaging*, vol. 27, no. 4, pp. 557–568, 2008.

[26] T. Mansi, S. Durrleman, B. Bernhardt, M. Sermesant, H. Delingette, I. Voigt, P. Lurz, A. M. Taylor, J. Blanc, Y. Boudjemline, X. Pennec, and N. Ayache, "A Statistical Model of Right Ventricle in Tetralogy of Fallot for Prediction of Remodelling and Therapy Planning," in *Medical Image Computing and Computer Assisted Intervention (MICCAI)*, ser. Lecture Notes in Computer Science, vol. 5761. London, UK: Springer, Sep. 2009, pp. 214–221.

[27] E. Rodriguez, A. Hoger, and A. McCulloch, "Stress-dependent finite growth in soft elastic tissues," *Journal of biomechanics*, vol. 27, no. 4, pp. 455–467, 1994.

[28] L. Geerts-Ossevoort, "Cardiac myofiber reorientation: A mechanism for adaptation," Ph.D. dissertation, Technische Universiteit Eindhoven, 2002.

[29] W. Kroon, T. Delhaas, T. Arts, and P. Bovendeerd, "Constitutive modeling of cardiac tissue growth," in *Functional Imaging and Modeling of the Heart*, ser. Lecture Notes in Computer Science, vol. 4466. Springer, 2007, p. 340.

[30] M. Beg, P. Helm, E. McVeigh, M. Miller, and R. Winslow, "Computational cardiac anatomy using MRI," *Magnetic resonance in medicine: official journal of the Society of Magnetic Resonance in Medicine/Society of Magnetic Resonance in Medicine*, vol. 52, no. 5, p. 1167, 2004.

[31] A. Qiu, L. Younes, M. Miller, and J. Csernansky, "Parallel transport in diffeomorphisms distinguishes the time-dependent pattern of hippocampal surface deformation due to healthy aging and the dementia of the alzheimer's type," *NeuroImage*, vol. 40, no. 1, pp. 68–76, 2008.

[32] P. Aljabar, K. Bhatia, M. Murgasova, J. Hajnal, J. Boardman, L. Srinivasan, M. Rutherford, L. Dyet, A. Edwards, and D. Rueckert, "Assessment of brain growth in early childhood using deformation-based morphometry," *Neuroimage*, vol. 39, no. 1, pp. 348–358, 2008.

[33] S. Durrleman, X. Pennec, A. Trouvé, G. Gerig, and N. Ayache, "Spatiotemporal atlas estimation for developmental delay detection in longitudinal datasets," in *Medical Image Computing and Computer Assisted Intervention (MICCAI)*, ser. Lecture Notes in Computer Science. Springer, 2009, pp. 297–304.

[34] B. Bernhardt, K. Worsley, H. Kim, A. Evans, A. Bernasconi, and N. Bernasconi, "Longitudinal and cross-sectional analysis of atrophy in pharmacoresistant temporal lobe epilepsy," *Neurology*, vol. 72, no. 20, p. 1747, 2009.

[35] S. Wold, M. Sjöström, and L. Eriksson, "Pls-regression: a basic tool of chemometrics," *Chemometrics and intelligent laboratory systems*, vol. 58, no. 2, pp. 109–130, 2001.

[36] K. Worsley, "An overview and some new developments in the statistical analysis of PET and fMRI data," *Human Brain Mapping*, vol. 5, no. 4, pp. 254–258, 1997.

[37] A. McIntosh and N. Lobaugh, "Partial least squares analysis of neuroimaging data: applications and advances," *Neuroimage*, vol. 23, pp. S250–S263, 2004.

[38] N. Ablitt, J. Gao, J. Keegan, L. Stegger, D. Firmin, and G. Yang, "Predictive cardiac motion modeling and correction with partial least squares regression," *IEEE transactions on medical imaging*, vol. 23, no. 10, pp. 1315–1324, 2004.

[39] A. Rao, P. Aljabar, and D. Rueckert, "Hierarchical statistical shape analysis and prediction of sub-cortical brain structures," *Medical Image Analysis*, vol. 12, no. 1, pp. 55–68, 2008.

[40] M. Vaillant and J. Glaunes, "Surface matching via currents," in *Proc. IPMI 2005*. Springer, 2005, p. 381.

[41] R Development Core Team, *R: A Language and Environment for Statistical Computing*, R Foundation for Statistical Computing, Vienna, Austria, 2009, ISBN 3-900051-07-0. [Online]. Available: http://www.R-project.org

[42] H. Akaike, "A new look at the statistical model identification," *IEEE transactions on automatic control*, vol. 19, no. 6, pp. 716–723, 1974.

[43] D. DuBois and E. DuBois, "The measurement of the surface area of man," *Archives of Internal Medicine*, vol. 15, no. 5_2, p. 868, 1915.

[44] R. Rosipal and N. Krämer, "Overview and recent advances in partial least squares," *Subspace, Latent Structure and Feature Selection*, pp. 34–51, 2006.

[45] H. Hotelling, "Relations between two sets of variates," *Biometrika*, vol. 28, no. 3-4, p. 321, 1936.

[46] Y. Fujikoshi and L. Veitch, "Estimation of dimensionality in canonical correlation analysis," *Biometrika*, vol. 66, no. 2, pp. 345–351, 1979.

[47] Y. Zheng, A. Barbu, B. Georgescu, M. Scheuering, and D. Comaniciu, "Four-chamber heart modeling and automatic segmentation for 3-D cardiac CT volumes using marginal space learning and steerable features," *IEEE Transactions on Medical Imaging*, vol. 27, no. 11, pp. 1668–1681, 2008.

[48] L. Yang, B. Georgescu, Y. Zheng, D. Foran, and D. Comaniciu, "A fast and accurate tracking algorithm of left ventricles in 3D echocardiography," in *Proceedings/IEEE International Symposium on Biomedical Imaging: from nano to macro. IEEE International Symposium on Biomedical Imaging*, vol. 5. NIH Public Access, 2008, p. 221.

[49] Z. Tu, "Probabilistic boosting-tree: Learning discriminative models for classification, recognition, and clustering," in *IEEE International Conference on Computer Vision, 2005. ICCV 2005*, vol. 2, 2005.

[50] K. Arun, T. Huang, and S. Blostein, "Least-squares fitting of two 3-D point sets," *IEEE Transactions on Pattern Analysis and Machine Intelligence*, vol. 9, no. 5, pp. 698–700, September 1987.

[51] P. Lurz, J. Nordmeyer, L. Coats, A. Taylor, P. Bonhoeffer, and I. Schulze-Neick, "Immediate clinical and haemodynamic benefits of restoration of pulmonary valvar competence in patients with pulmonary hypertension," *Heart*, vol. 95, no. 8, p. 646, 2009.

[52] T. Mansi, "Image-Based Physiological and Statistical Models of the Heart, Application to Tetralogy of Fallot," Thèse de sciences (PhD Thesis), Ecole Nationale Supérieure des Mines de Paris, September 2010.

[53] L. Mei, M. Figl, A. Darzi, D. Rueckert, and P. Edwards, "Sample Sufficiency and PCA Dimension for Statistical Shape Models," in *Proc. ECCV*, ser. Lecture Notes in Computer Science. Springer, 2008, pp. 492–503.

[54] J. Rice, *Mathematical Statistics and Data Analysis*. Duxbury Press Belmont, CA, 1995, vol. 2.

[55] F. Faul, E. Erdfelder, A. Lang, and A. Buchner, "G* Power 3: A flexible statistical power analysis program for the social, behavioral, and biomedical sciences," *Behavior Research Methods*, vol. 39, no. 2, p. 175, 2007.

[56] A. Rao, G. Sanchez-Ortiz, R. Chandrashekara, M. Lorenzo-Valdes, R. Mohiaddin, and D. Rueckert, "Comparison of cardiac motion across subjects using non-rigid registration," in *Medical Image Computing and Computer Assisted Intervention (MICCAI)*, ser. Lecture Notes in Computer Science. Springer, 2002, pp. 722–729.

[57] M. DoCarmo, *Riemannian Geometry (transl. by Francis Flaherty), Math. Theory Appl*. Birkhäuser Boston, Inc., Boston, MA, 1992.

[58] A. Frigiola, V. Tsang, J. Nordmeyer, P. Lurz, C. van Doorn, A. Taylor, P. Bonhoeffer, and M. de Leval, "Current approaches to pulmonary regurgitation," *European Journal of Cardio-Thoracic Surgery*, vol. 34, no. 3, p. 576, 2008.

[59] D. Tang, C. Yang, T. Geva, and J. Pedro, "Patient-specific MRI-based 3D FSI RV/LV/patch models for pulmonary valve replacement surgery and patch optimizationPatient-specific MRI-based 3D FSI RV/LV/patch models for pulmonary valve replacement surgery and patch optimization," *Journal of biomechanical engineering*, vol. 130, p. 041010, 2008.

[60] T. Mansi, B. André, M. Lynch, M. Sermesant, H. Delingette, Y. Boudjemline, and N. Ayache, "Virtual pulmonary valve replacement interventions with a personalised cardiac electromechanical model," in *Recent Advances in the 3D Physiological Human*, ser. Lecture Notes in Computer Science. Springer, 2009, vol. 5528, pp. 201–210.